ADVANCED ENERGY MATERIALS
www.advenergymat.de

Controlling Sodium Dendrite Growth via Grain Boundaries in $Na_3Zr_2Si_2PO_{12}$ Electrolyte

Zhonghui Gao, Yang Bai, Junrun Feng, Jiayi Yang, Porun Liu, Haiyang Yuan, Xuze Guan, Feng Ryan Wang, and Yunhui Huang**

$Na_3Zr_2Si_2PO_{12}$(NZSP)-based NASICON solid-state electrolytes (SSEs) show not only competitive ionic conductivity but also high chemical stability in air, holding a great promise for enabling the use of sodium metal anode in solid-state sodium batteries. However, sodium (Na) metal dendrite growth inside SSE always leads to undesirable short-circuiting in battery even no obvious changes in interfacial contact loss and interfacial decomposition during cycling. How to control Na metal dendrite growth and in situ observe the effect of SSE/Na interface change on dendrite growth is quite challenging. Herein, an in situ synchrotron-based X-ray imaging method is developed to systematically investigate the dendrite origin in NZSP-based SSEs. It is find that the dendrite growth intrinsically depends on the grain boundaries (GBs) in NZSP and the NZSP/Na interfacial properties. It is confirmed that Na dendrite infiltration kinetic evolution in NZSP is strongly associated with Na ion/electron conductivity and Young's modulus of GBs. Moreover, the electro-chemo-mechanical phase-field model evaluation demonstrates that the basic reason for Na metal dendrite intrusion into the GBs of SSE is a combination of local polarization potential and the presence of stress formed at GBs.

1. Introduction

Solid-state batteries with solid-state electrolytes (SSEs) are currently considered as next-generation electrochemical devices to achieve both high energy density and safety.[1–3] The current research mainly focuses on solid-state lithium (Li) batteries, but by concerning about the availability of Li resource triggered by the huge demands of current and future Li-based battery markets, developing other rechargeable batteries as technical reserve is desirable, in particular solid-state sodium (Na) batteries.[4,5] Moreover, very abundant and convenient sodium resources make solid-state Na batteries very attractive for the potential large-scale application market compared to solid-state Li batteries.[6] $Na_3Zr_2Si_2PO_{12}$ (NZSP) ceramic SSE has a high ionic conductivity up to 10^{-3} S cm^{-1} (25 °C) and shows a stable interface performance when it contacts with metallic Na.[7,8] However, Na dendrite growth or filament penetration during cycling at high current density is always found in solid-state Na batteries, which shows a similar behavior to solid-state Li batteries.[9,10] There are many studies focusing on the Li dendrite in solid-state Li batteries but few on Na dendrite.[11] We can use the principles based on Li dendrite for reference to guide the corresponding research for solid-state Na batteries. Prior results have demonstrated that the interface contact is the major motivation for Li dendrite or filaments propagation or dendrite initiation at the SSEs/Li interface.[12,13] Thus, numerous methods have been employed to improve SSE/Li (Na) interface issues. The typical one is

Z. Gao
School of Materials Science and Engineering
Tianjin University
Tianjin 300350, China

Z. Gao
School of Materials Science and Engineering
Tongji University
Shanghai 201804, China

Y. Bai
Microstructure Physics and Alloy Design
Max-Planck-Institut für Eisenforschung
40237 Düsseldorf, Germany

J. Feng, X. Guan, F. R. Wang
Department of Chemical Engineering
University College London
Roberts Building, Torrington Place, London WC1E 7JE, UK
E-mail: ryan.wang@ucl.ac.uk

J. Yang, Y. Huang
School of Materials Science and Engineering
Huazhong University of Science and Technology
Wuhan, Hubei 430074, China
E-mail: huangyh@hust.edu.cn

P. Liu
Centre for Clean Environment and Energy
Griffith University
Gold Coast, Queensland 4222, Australia

H. Yuan
School of Materials Science and Engineering
East China University of Science and Technology
Shanghai 200237, China

The ORCID identification number(s) for the author(s) of this article can be found under https://doi.org/10.1002/aenm.202304488

DOI: 10.1002/aenm.202304488

to introduce a protection layer, such as Al_2O_3, TiO_2, and Sn, between the metallic Li (Na) with the SSEs.[14–16] In addition, several chemical/physical treatments of the SSEs have also been used to uniform the current distribution at the interface, which is believed to be crucial to suppress dendrite formation.[17,18]

Although the above-mentioned SSE/Li (Na) interface issues can be improved by using the methods like protection coating and isostatic pressing treatment,[19] dendrites are always found to form and propagate in SSE and grow through the SSE when the solid-state cell runs at above critical current density, resulting in short-circuiting of the battery. On the one hand, the dendrite growth may drive cracks to propagate within SSE because of the formed inhomogeneous stress, and the newly formed cracks provide the vacant space for dendrites to grow further.[20] On the other hand, the metal dendrites can grow along the GBs network and contact with each other in SSE.[21] To address the dendrite issue, it is necessary for us to well understand the GBs properties. The GBs in a real SSE are often interfaces of two randomly oriented grains.[22,23] The growth of a dendrite and its network formation along the GBs involve multiple factors of GBs, such as the mechanical property, electronic and ionic conductivity. The inhomogeneity of mechanical property of the SSE due to the difference between grains with GB may lead to a nonuniform stress distribution, and may potentially trigger uneven Li (Na) deposition.[24–27] In addition to the mechanical consideration, the excess electrons trapped in GBs are believed as the viable cause for the isolated Li nucleation and growth in the bulk SSEs.[28] A recent experimental work demonstrates that LLZO GBs show a narrowed bandgap of 2.2 eV, which can promote the dendrite or filament formation.[21] Han et al. reported that the LLZO has a high electronic conductivity measured by neutron depth profiling.[29] The macroscopic characterizations show that the electronic conductivity of LLZO cannot identify the isolated role of GBs contribution to the electronic conductivity.[30–32]

Clarifying the effect of GB properties on metal dendrite growth is crucial for increasing CCD of the solid-state battery. For SSEs, it is very hard to evaluate the real electrochemical environments of GBs during galvanostatic cycling, and how the local potential, ion concentration, and mechanical properties change at GBs dependent on the applied galvanostatic values during cycling? Resolving these issues is challenging, because the GBs are always coupled with electrochemical-mechanical behaviors and the SSE/Li interface properties are always considered as the general motivations for dendrite initiation and propagation. In this work, we provide answers to above-mentioned questions by combining in situ synchrotron-based X-ray characterization, electrochemical measurements with the electro-chemo-mechanical phase-field (PF) model. We demonstrate that Na dendrite initiate within the NZSP and grow along GBs and we also give quantitative results on how the interplay between mechanical and ionic/electronic properties of the GB impacts on the Na penetrant kinetics and penetration morphologies. We further provide a model validated by experiments, which can predict quantitatively how the GB properties including Na penetrant morphology and evolution, potential, and mechanical stress varies with applied galvanostatic values. These findings have been used to guide the synthesis of the SSEs with suitable GBs structure for Na dendrite suppression, altering the synthesis strategies to increase the density of NZSP (by reducing porosity), increase the grain size and/or improve contact at the GBs. The proposed mechanism rationalizes novel guidelines to improve the GB properties and suggests to create more resilient SSEs for solid-state sodium battery.

2. Results and Discussion

A symmetric Na/NZSP/Na cell was designed and isostatic pressing was applied for the NZSP/Na interface kinetics measurement to avoid the impact of poor interface contact and the gradual contact loss formed during stripping. The pressure perpendicular to the NZSP/Na interface was altered via a screw and a spring. **Figure 1a** shows that the polarization voltage of the symmetric cell increases gradually with applied current density and becomes fluctuating when the current density reaches 0.3 mA cm^{-2}. The voltage fluctuation becomes more severe with increasing the current density especially when the current is higher than 0.45 mA cm^{-2}. The voltage increase is mainly ascribed to the inhomogeneous distribution of Na ions around the GBs, while the voltage reduction of is mainly attributed to the electrons in the GB leakage current, which induced by a sufficiently large current density (>0.3 mA cm^{-2} in this work). Decreasing the local potential can sufficiently reduce Na ions into Na metal.[33–34] Figure 1c shows the Nyquist plots of the impedance spectra recorded operando during plating-stripping cycling with different current densities for ideally contacted NZSP/Na interfaces at room temperature (25 °C). The impedance response includes bulk and grain boundary (inserted in Figure 1c)[35] contributions, and the impedance gradually decreases with increasing current density. When a constant current density of 0.3 mA cm^{-2} is applied, the polarization voltage begins to decrease (Figure 1a), which indicates that the continuous Na infiltration into the NZSP before the short circuit occurs. When the applied current density continues to increase, the polarization voltage begins to fluctuate, indicative of continuous Na-ion accumulation and dendrite growth along GBs. At the meantime, the bulk resistance of the NZSP decreases from 320 to 254 Ω according to the EIS fitting results (Figure 1b), which demonstrates the Na metal dendrites gradually penetrate and grow in NZSP during cycling. That is because the metallic Na inside NZSP can significantly improve the electronic conductivity of NZSP. The bulk resistance reduction of NZSP corresponding to EIS is attributed to the increase in carriers (electron and Na ion) concentration. Large enough current density will lead to continuous Na deposition and growth along GBs and eventually cause short circuiting. For the R_{int} of NZSP/Na, it decreases dramatically after cycling from ≈ 220 to 21 Ω cm^2 (Figure 1d). This behavior can be attributed to an additional increase in effective contact area (load-bearing contact area) between the NZSP grains and the Na metal formed at GBs. It is noteworthy that the contact interface between NZSP pellet with Na metal electrode was almost electrochemically stable after we disassembled the cell that had already been short-circuited (**Figure 2**). Thus, the Na metal electrode/NZSP contact interface is not the main motivation for the reduction of $R_{int.}$ The details for the NZSP/Na metal interface reaction mechanism during cycling at different current densities will be discussed in **Figures 3** and **4**.

The NZSP pellet was further examined after a Na/NZSP/Na symmetric IXIcell was cycled under galvanostatic conditions till

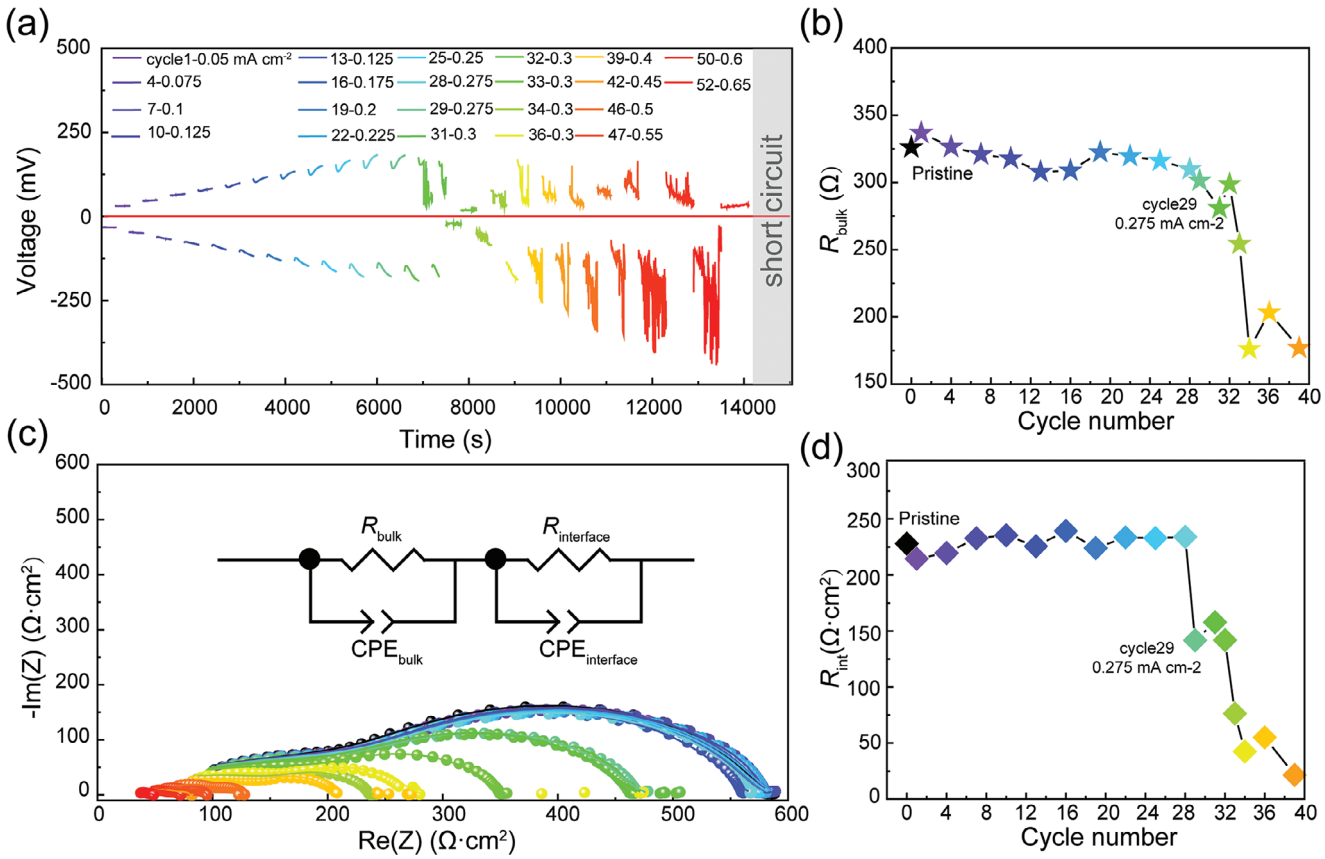

Figure 1. The d.c. cycling performance and the corresponding EIS curves of symmetric Na/NZSP/Na cell. a) The d.c. cycling performance at room temperature (25 °C) by stepping the current density from 0.05 to 0.65 mA cm^{-2}. The curves with different colors correspond to the potential and current density. c) Evolution of the Na/NZSP/Na cell Nyquist plots with cycles corresponds to the different current densities, respectively. The Nyquist plot was collected after each charging-discharging cycle with corresponding current density. (b and d) The fitted impedance of $R_{bulk\ NZSP}$ and $R_{Na/NZSP}$ contributions obtained from the analysis of the impedance spectra (c). All measurements were performed on symmetric Na/NZSP/Na cell with a constant pressure.

the critical current density (CCD) was exceeded. The CCD was found to be 0.3 mA cm^{-2} at room temperature (Figure 1a). The NZSP pellet disassembled from the IXIcell shows dark spots and lines at its surface (Figure 2b). The dark locations are caused by Na dendrites infiltrating the NZSP pellet, leading to short circuit of the cell. Figure S1 (Supporting Information) shows the distinct NZSP cross-sectional fracture surface, from which we can see the trajectory of the Na spots following the Na-ion current path between NZSP and Na metal electrode. The SEM image clearly shows that Na dendrite penetrate into NZSP. Figures 2d–g displays the SEM images of the NZSP pellet surface and cross-section as well as corresponding EDS mappings for the short-circuited cycled Na/NZSP/Na cell. For the pores in NZSP, the onset of Na metal deposition in grain boundaries of NZSP can progress into the connected pores. The grain boundaries and voids of NZSP are penetrated by needle like and blade like metallic Na. This indicates that the Na dendrites prefer to nucleate and grow along the GBs and voids of the NZSP pellet.[36] The growth of the Na dendrite provides more intimate contact area between NZSP grains and Na, leading to decrease in voltage and R_{int} during the CCD process, as shown in Figure 1. Figure 2h shows TEM image of the region selected for study, where three GBs are connected with a void at the junction. Although the change in the GB itself cannot be easily reflected in TEM, EDS mappings are used to characterize microscopic Na dendrite grow in NZSP. Figure 2i–m show that Na element is aggregated along the grains and GBs of NZSP after short circuit. This illustrates that Na ions can diffuse and accumulate along the GBs of NZSP and precipitate as trapped metallic Na. XPS analysis (Figure S2, Supporting Information) suggests that the dark linear spots or regions have a more Zr reduced character compared to the white or the white NZSP area in the cycled pellet.[37] This indicates that the formed Na metal can lead to local change in Zr environment. XPS analysis (Figure S3, Supporting Information) suggests that the white area of NZSP surface have no obvious changes for Na 1s, O 1s, P 2p and Si 2p regions before and after short circuit.

NZSP/Na interface structural change during the electrochemical cycling can affect Na dendrite growth. To evaluate the influence of NZSP/Na interface electrochemical properties on Na dendrite growth, the in situ micro-X-ray absorption near edge structure (μXANES) measurements were performed at the beamline I18 at the diamond light source (Harwell, UK). In situ representative features of NZSP/Na metal interface during cycling at different current densities are shown in Figure 3. The NZSP/Na

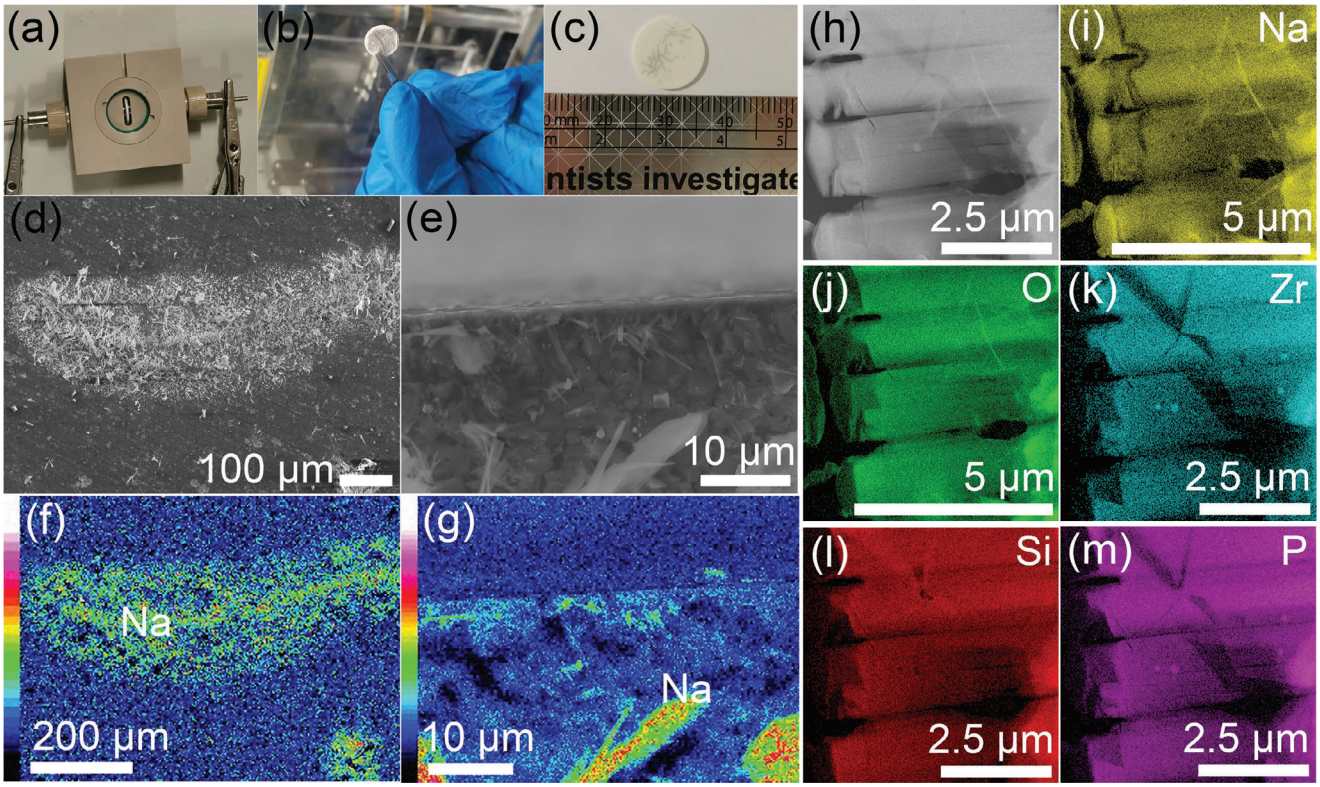

Figure 2. The d.c. cycling test of Na/NZSP/Na and microscopy images of short-circuited NZSP after dendrite penetration. a) Optical microscopy image of an in situ X-ray imaging cell (IXIcell). b) Optical microscopy image of NZSP pellet with metallic Na attachment disassembled from the IXIcell. c) Optical microscopy image of the cycled NZSP pellet, the black dendritic lines are the region where the short circuit occurred. d) and e) SEM image of the NZSP at the short-circuit region and its elemental EDX mapping of Na. f) and g) SEM image of the NZSP in a cross-section and its elemental EDX mapping of Na, showing the Na dendrite and blade structure along the GBs and voids. h–m) TEM image of NZSP at the short-circuited region after Focused Ion beam (FIB) treatment and its elemental EDX mapping of Na, O, Zr, Si and P, respectively.

contact interface was further examined after the Na/NZSP/Na IXIcell was cycled under galvanostatic conditions till the CCD was exceeded. The CCD was found in IXIcell to be 0.6 mA cm^{-2} at 25 °C (Figure 3a). Figure 3c shows the in situ IXIcell electrochemical design for synchrotron-based X-ray characterization. The optical image shows the interface between NZSP (grey area) and Na metal (metallic luster area). The high sensitivity and resolution of XANES provides an excellent imaging tool to study microscale chemical changes or evolution. We conducted 2D grid scans with the beam (size 2.0 μm × 2.5 μm) at different energy points, which produced a series of fluorescence images. A surprising observation for NZSP/Na interface after cycling is that the regions of interphase layer are formed and visible, as shown in Figure 3d. Zr K-edge XANES maps with different colors show that there is a new Zr-based phase (green area) in this area of the NZSP/Na interface. Moreover, the new formed green region at NZSP/Na interface does not show any significant change with stepping the current density from 0.05 to 0.3 mA cm^{-2}, even after a short circuit.[38] This is because the new interphase formed at NZSP/Na interface is stable, which can protect the NZSP electrolyte from continuous reduction by metallic Na or other electrochemical reactions. The Zr K-edge XANES spectra corresponding to NZSP and NZSP/Na interface are notably different for phase identification through XANES mapping (Figure 4). We also identified the possible phase equilibria and decomposition reaction energies of sodiation and desodiation of NZSP against Na, as shown in Figure S4 (Supporting Information). Our DFT computation results determine that the thermodynamically favorable decomposition formed interphase mainly consists of Na_2O, Na_2O_2, NaSi and Na_3P, which can function as a passivating layer for NZSP during cycling.[37,39,40]

The XANES spectra and their corresponding first derivatives of NZSP and the interphase formed at NZSP/Na interface are shown in Figure 4b–e. For the NZSP/Na interface, with increasing the cycling current density, the main absorption edge clearly shifts to a lower energy. This clear trend in the XANES spectra implies the occurrence of Zr reduction during cycling.[41] In Figure 4b, Zr K-edge XANES spectra of the bulk of NZSP do not change obviously with stepping the current density from 0.05 to 0.6 mA cm^{-2} after 6 cycles, even after a short circuit. Additionally, there is no pre-edge feature at about 18 005 eV corresponding to a 1s-4d transition, which is only allowed if there is some p-d mixing. The pre-edge structure that is most apparent in tetragonal phase is also lacked in first derivative plots. This indicates that the pre-edge of NZSP shows feature similar to the octahedral coordination of Zr-O, because the 1s-4d transition is very weak for the centrosymmetric coordination geometries like in octahedral ZrO_6.[42] The edge width, which can be observed in the first derivative, can be used to determine the width of the valence band.[43] The large edge width of NZSP indicates the high

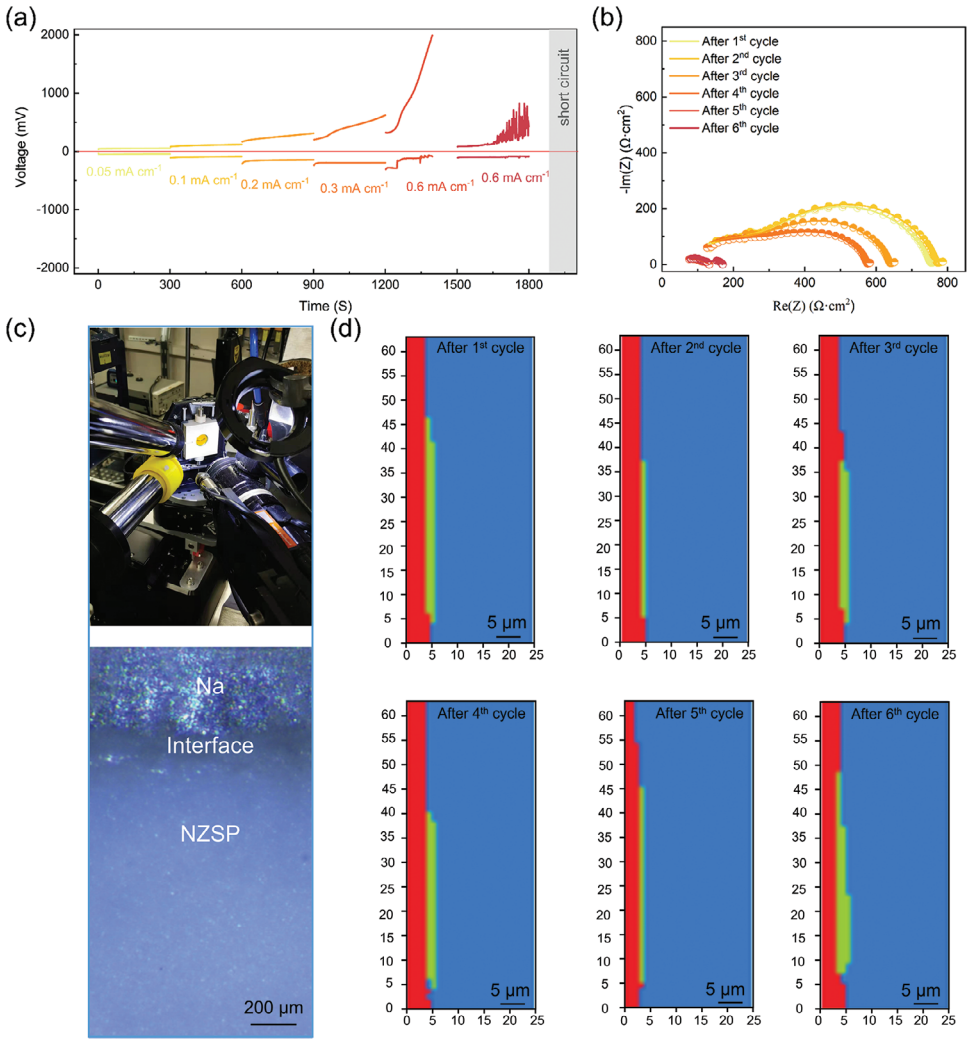

Figure 3. In situ observation of the electrochemical stability of NZSP/Na interface during cycling. a) The d.c. cycling of Na/NZSP/Na IXIcell at 25 °C by stepping the current density from 0.05 to 0.6 mA cm^{-2}. b) Nyquist plots of Na/NZSP/Na after each cycling. c) The measuring instrument and optical microscopy image of the Na/NZSP interface; the metallic luster and grey area correspond to the Na metal and NZSP, respectively. d) XANES mapping (25 × 63 μm) of Zr K-edge at NZSP/Na interface correspond to each cycling. The green area represents the new Zr-based phase in this area of the NZSP/Na interface, the blue area represents the bulk Zr of NZSP, and the red area represents the Na metal side.

covalency for Zr—O bond.[44] These results demonstrate that NZSP is electrochemical stable with Na metal during the CCD cycling, and the continuous electrochemical reaction during cycling is not observed. Qualitative information can be obtained by comparing XANES spectra with those of mapping areas, which clearly show that the stable interphase formed at NZSP/Na interface can protect NZSP from the continuous chemical/electrochemical reactions with Na metal. Thus, we deduce that the growth of Na metal dendrite in NZSP may involve multiple factors, such as the NZSP/Na interface properties and the GBs properties. In addition to the influence of NZSP/Na interface electrochemical changes, the dynamically evolving local electric potential and mechanical properties of NZSP GBs are the main motivation for dendrite growth in NZSP in this study.

The above experimental results have shown that Na metal dendrites mainly penetrate stiff NZSP pellet along its GB network, resulting in cell failure. Detecting the local potential change at the GB and monitoring the kinetics of Na dendrite growth during cycling are big challenges due to the combined influence of electrochemical-mechanical coupling and complicated conditions. To illustrate the distributions of various fields (i.e., Na ion concentration and Na metal dendrite patterns), we initiate the simulation by artificially inducing nucleation (circular dendrite dot with a radius around 50 nm) at the center of the NZSP grains. Taking into account the great influence of the Na ion conductivity and Young's modulus of GBs on both the growth rate of Na dendrites and their resulting morphologies, the simulation has explored various values for these properties. It is important to highlight that a 5% volume expansion is assumed during Na metal dendrite growth. All simulations employ an identical microstructure, characterized by the same number of grains and same geometry of the grain boundaries (GB). The investigation varies properties of the GB while maintaining this uniform GB geometry. It should be noted that this work focuses solely on the

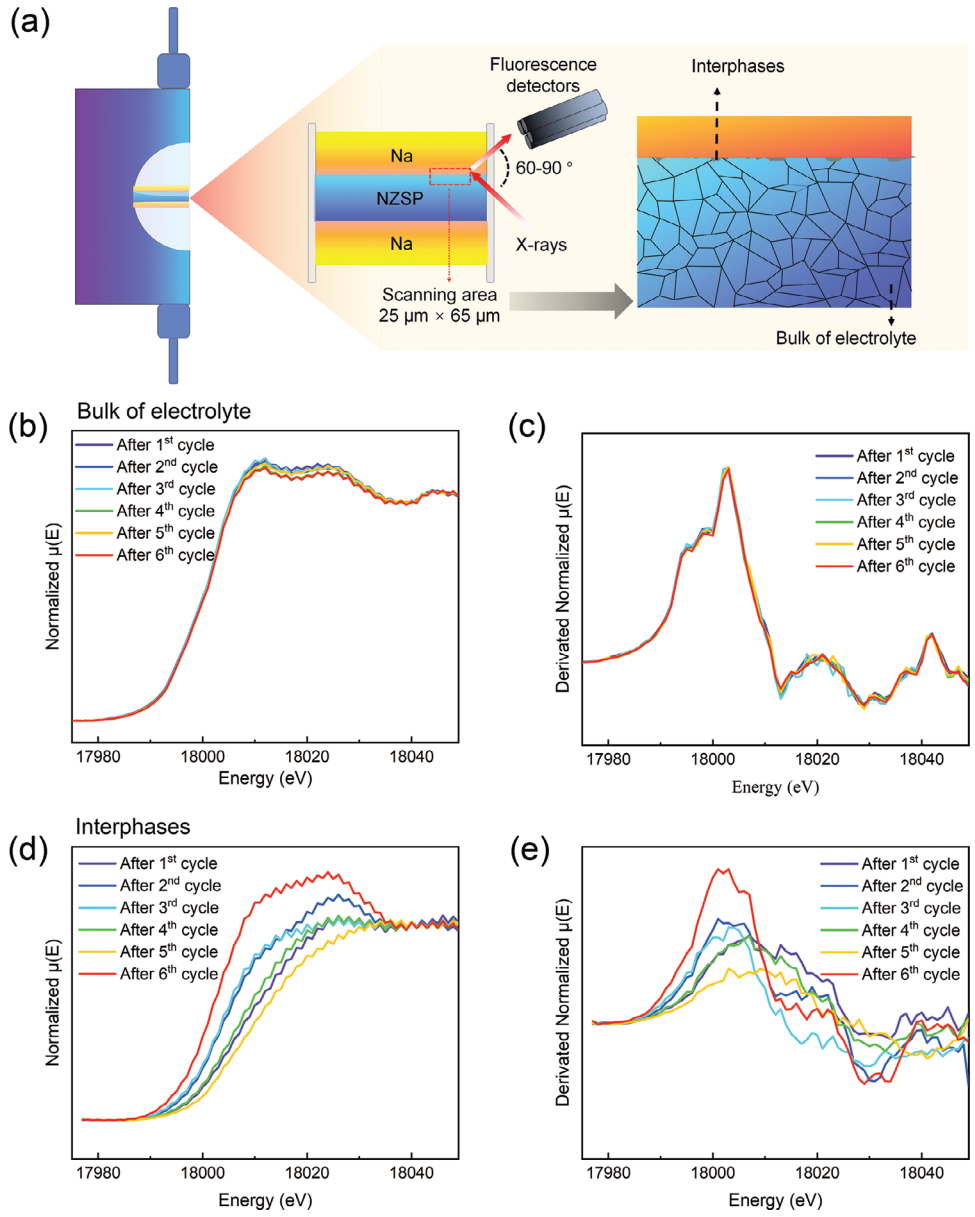

Figure 4. XANES spectra Zr K-edge for Na/NZSP interface after each cycling. a) Schematic in situ electrochemical cell design and for Na/NZSP/Na interface characterization in this study. b,c) The XANES spectra of Zr K-edge and their corresponding first derivatives of the NZSP. d,e) The XANES spectra of Zr K-edge and their corresponding first derivatives of the interphase formed at NZSP/Na interface during cycling. The XANES spectra of Zr K-edge were smoothened by using *Athena* because low concentration of the formed interphase shows a high noise-signal ratio.

lithiation process. Nonetheless, simulating the lithiation/delithiation cycle can be readily achieved by simply altering the boundary conditions.

Figure 5 displays the localized variations of Na ion concentration, electric potential, current, and stress change corresponding to different Young's modulus of GB. The growth of Na dendrites at GBs can be attributed to the differences in both Young's modulus and Na ion concentration between the GBs and the grains of NZSP. The growth of Na dendrites results in volume expansion, which subsequently impacts the von Mises stress within the grains and at grain boundaries. Recalling Equation 15, the variation in stress distribution gives rise to different driving forces for dendrite growth. However, Figure 5 indicates that the ultrasoft nature of Na metal and its extremely low yield stress can significantly decrease the stress, resulting in low stress level (70 MPa) for NZSP. Additionally, despite a significant change in the Young's modulus of GB (1 GPa, 20 GPa, 50 GPa, and 80 GPa), there is only a minimal difference observed in the effective plastic strain and von Mises stress, as demonstrated in Figure 5f. As a consequence, the low stress has a limited impact on dendrite growth, resulting in similar dendrite patterns across all samples, as depicted in Figure 5a and b. The tip interfaces between Na metal dendrite with GBs have higher concentration and electric potential gradient (potential difference

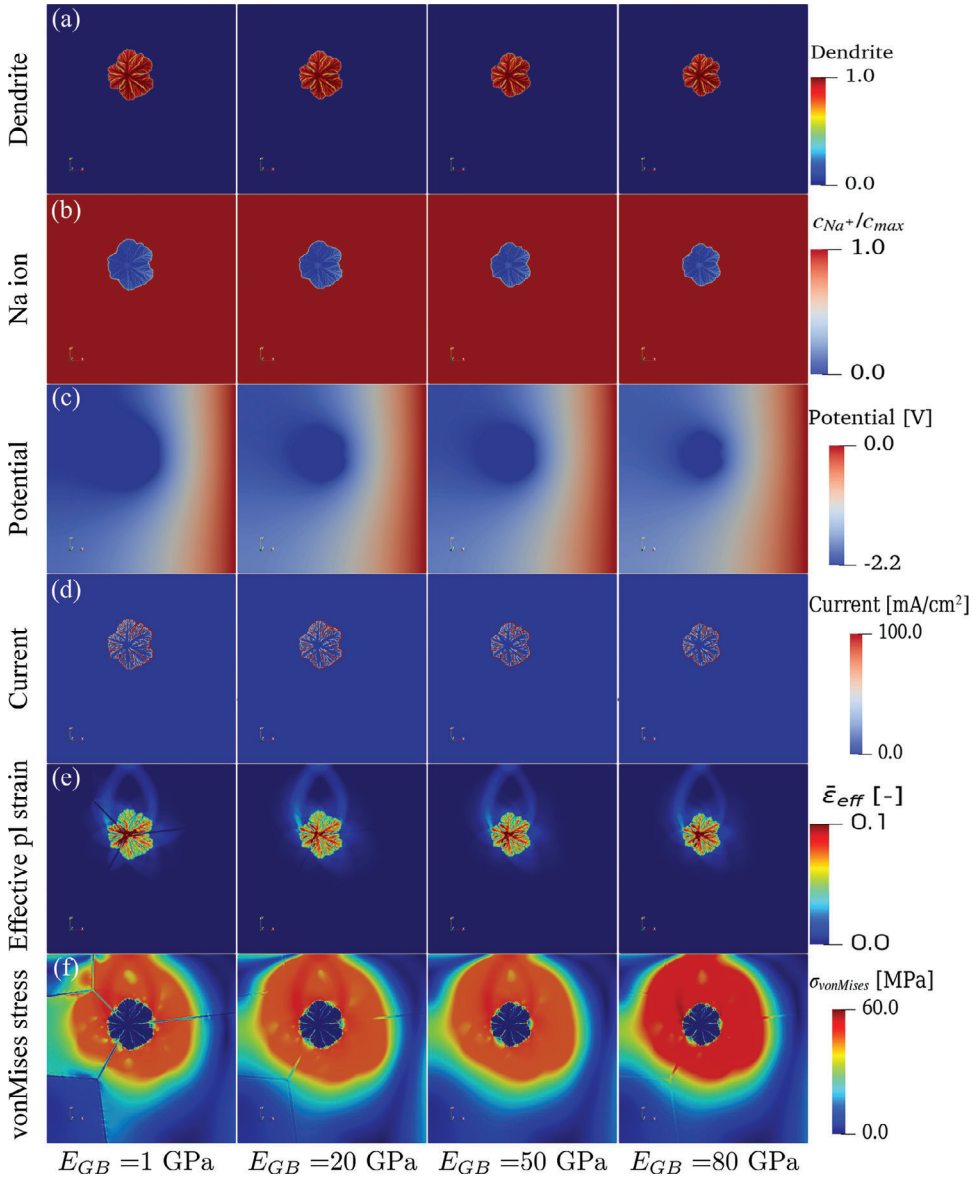

Figure 5. Effect of Young's modulus of GBs on dendrite growth. a) The sequence from top to bottom displays dendrite growth at $t \approx 0.05$ s, followed by the b) distribution of Na ions, c) electric potential, d) current density, e) effective plastic strain, and f) the vonMises stress of the sample with varying GB stiffness.

across the interface), which can give larger driving force for their faster growth. Thus, all cases exhibit a comparable high current density (≈ 400 mA cm^{-2}) at the interface between the Na metal dendrite phase and GB phase, as shown in Figures 5d and 6a. The potential changes at the Na dendrite/GBs interface with different modulus are shown in **Figure 6**b. The faster the slope of the interface potential decrease, the faster reaction rate at which Na ions are electrochemically reduced to metallic Na. Figure 6b indicates that GBs with high modulus can inhibit Na dendrite growth based on Equation 15. According to the modeling results (Figures 5 and 6), the Na metal dendrite preferentially grows along the GBs with lower Young's modulus, which is due to the low mechanical stress level in the driving force. Furthermore, we should note that the potential and stress formed across the Na/GB interface play important roles in directing the Na metal dendrite growth rate and morphology evolution.

During the charge/discharge process in NZSP, the Na-ion conductivity of GBs primarily affects the distribution of electric potential and the rate of Na dendrite growth along the GBs. The potential formed at GBs of NZSP have a more significant change under a lower GBs Na-ion conductivity. Because a smaller Na ion conductivity leads to larger GB resistance of NZSP, which indicates that under the same current density, a higher potential can be observed. **Figure 7** shows the snapshots of the metallic Na dendrite, Na-ion concentration, electric potential, current, and von Mises stress distributions at NZSP GBs as a function of varying Na ion conductivity of GBs.

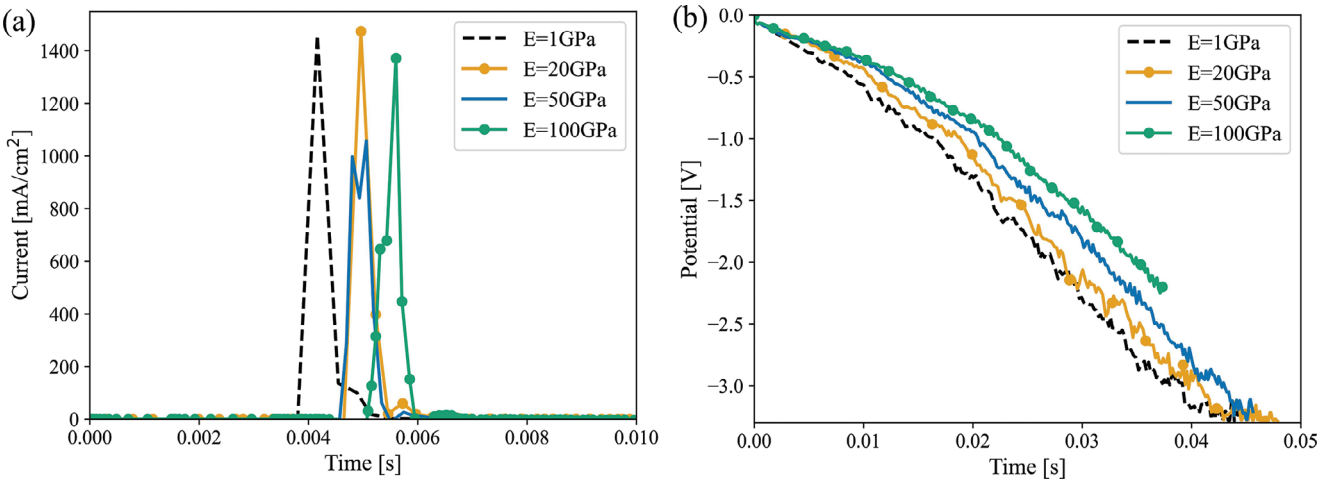

Figure 6. a) Depicts the variation in current density at the selected point over time for different E_{GB}, b) illustrates the change in potential at this point over time for different cases.

As shown in Figure 7, the concentration gradient decreases as ionic conductivity increases (no concentration gradient captured at the GB). According to Equation 9, higher Na-ion concentration can contribute to a larger reaction rate. Consequently, NZSP samples with lower ionic conductivity may lead to greater concentration gradient and higher occurrence of dendrite formation. A typical fiber-like pattern with small branches is captured in Figure 7a. Further increasing the GB Na-ion conductivity, corresponding to a large driving force due to the high Na ion concentration, even promotes the tendency of tips to split.

It is evident to see from Figure 7c that higher GB Na-ion conductivity results in less potential change along GBs and across the Na metal dendrite/NZSP phase interface. For instance, in the case with $\bar{\sigma}_{GB}$= 100 σ_{GB} (σ_{GB} = 0.25 S/m), the potential is almost uniform (0.1 mV), while in the other cases ($\bar{\sigma}_{GB}$= 0.05 σ_{GB} and $\bar{\sigma}_{GB}$= 0.1 σ_{GB}), a potential change span of −2.5 V is observed, as shown in the first column in **Figure 7c**. GBs in SSEs generally exhibit poorer electronic conductivity compared to the bulk material. The fluctuation of local GB potential could lead to the leakage because of the low work function (2.4 eV) of NZSP measured by UPS (Figure S5, Supporting Information. Additionally, when the applied current density is large enough to reduce the GB potential below 0 V, GBs will serve as the channels for Na metal deposition. In such cases, electrons tend to preferentially flow through the GBs, thereby promoting the reduction reaction of Na ions (dendrite growth). The concentration gradient of local Na ions decreases as Na-ion conductivity increases (the blue region disappears in Figure 7b). GBs with lower Na-ion conductivity can result in a larger number of dendrites, as illustrated in the first row of Figure 7a. This is because the lower GB Na ion conductivity leads to a higher Na-ion concentration gradient, which can enable a higher reaction rate based on Equation 12. The rapid growth of metallic Na dendrites leads to significant NZSP GB/Na dendrites interface potential fluctuations at GB, as shown in Figure 7c. The Na/NZSP interface current at GB mainly depends on the potential gradient based on Equation 18. Figure 7d shows that with larger Na-ion conductivity, the current density at GBs region along dendrite branch become larger indicating a fact that Na dendrite growth is facilitated by the low GB Na ion conductivity. Moreover, the higher Na ion conductivity is able to homogenize Na ion concentration at GBs. In addition, the larger effective plastic strain in these cases supports the stronger reaction kinetics, leading to faster Na metal dendrite growth around the GBs, as shown in Figure 7e and f. However, the von Mises stress in all samples remains fairly low due to the extremely low yield stress of metallic Na, and no significant variation is observed.

The local point of current density and potential for NZSP GB/Na dendrite are shown in **Figure 8**. In Figure 8a, the high conductivity of GBs (blue line with triangle markers) enhances Na-ion diffusion, which results in a higher current than the other two cases based on the Ohm's law (Equation 18). Additionally, poor Na-ion conductivity causes a large potential change (Figure 8b). The solid yellow line and dark dashed line shows a potential change of around 2.5 V compared to the green and blue lines ($\bar{\sigma}_{GB}$= 100 σ_{GB} and $\bar{\sigma}_{GB}$= 10 000 σ_{GB}). That is because the different GB Na ion conductivity leads to the heterogeneous distribution of Na ion concentration at GB, thereby, significant potential change is formed along the GBs according to the Equation 15. According to the equation I_{BV}, large potential change can further impede Na-ion diffusion at localization of GB, resulting in faster Na-ion reduction and a larger number of dendrites. When the local potential at GBs surpasses the bandgap of NZSP, the GBs become incapable of impeding the flow of electrons (Figure S5, Supporting Information). Consequently, with the onset of leakage current, the GBs act as a source of electrons, further facilitating the growth of Na metal dendrites specifically at the grain boundaries.

Another important characteristic of GB that can affect the Na metal dendrite growth is Na-ion diffusivity. As shown in Figure S9 (Supporting Information), when the GB diffusivity is low, the diffusion of Na ions through the GB becomes difficult, resulting in the accumulation of Na ions around the GB. As a result, a lower GB diffusivity leads to faster and more pronounced Na metal dendrite growth. It can also affect the distribution of vonMises stress, plastic strain, and local current density at GBs. Collectively, these characteristics of GBs unveil two important findings. First, the varying Young's modulus and Na-ion conductivity of GBs

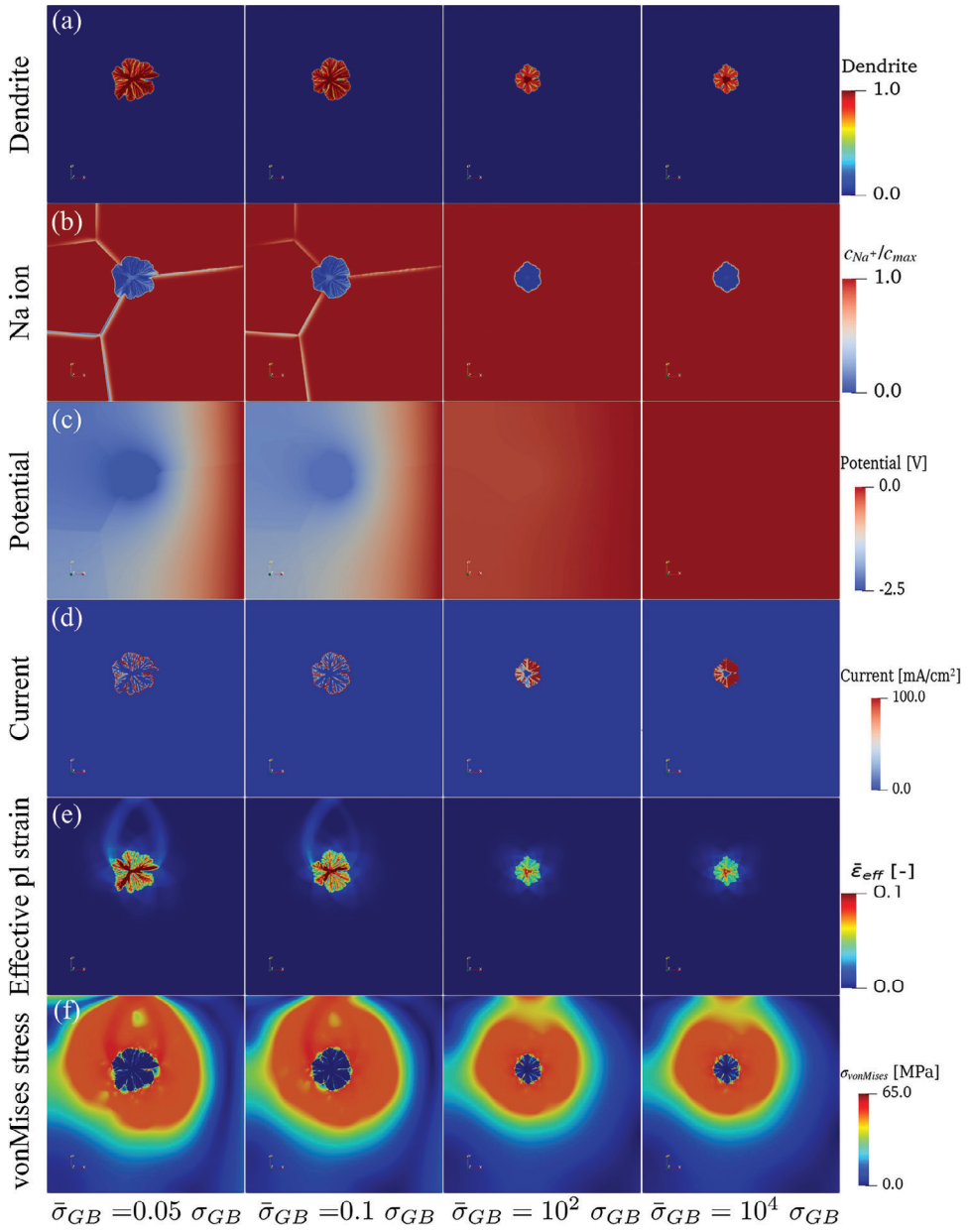

Figure 7. Effect of GB conductivity of NZSP on dendrite growth during electrochemically induced reaction. The sequence from top to bottom displays a) dendrite growth, followed by b) the distribution of Na ions, c) electric potential, d) current density, e) effective plastic strain, and f) the vonMises stress of the sample with varying GB conductivity. σ_{GB}= 0.25 S m^{-1} has been used in the simulation.

contribute to the non-uniform distribution of potential and Na-ion concentration within local regions of the GBs. Second, it is worth highlighting that GBs with distinct properties serve as favorable regions for the growth of Na metal dendrites within NZSP electrolyte pellets during cycling. For this model, our previous studies have shown that the GB resistance for Na ions depends on the GB structure and temperature.[34] The d.c. cycling of Na/NZSP/Na cells by stepping the current density from 0.06 to 0.25 mA cm^{-2} at 60 °C shows a better cycling stability than that at 25 °C (Figures S6 and S7, Supporting Information). Our studies also demonstrate that reduction of R_{GB} by increasing temperature and improving the Young's modulus with GB modifier can effectively suppress the Na metal dendrite growth,[34] which is apparently consistent with the simulated patterns in Figures 5 and 7. Moreover, our results demonstrated that reducing porosity and microscopic defects of NZSP, as well as altering its grain structure, is an effective strategy for increasing its CCD.[34]

3. Conclusion

The electrochemical stability of NZSP/Na interface and GB properties of NZSP are the main motivations for Na metal dendrite infiltration and the corresponding short circuit. We evaluate the influence of NZSP/Na interface electrochemical properties on

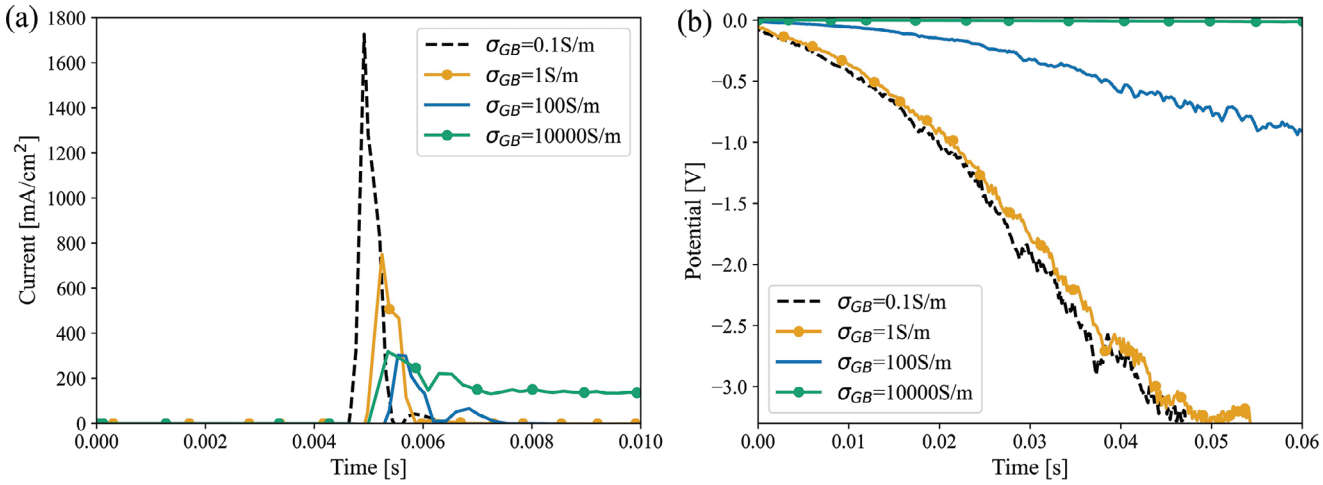

Figure 8. Displays the change in the local current density over time at the selected point in a), and the change in potential over time at the same point in b).

Na dendrite growth by in situ μXANES experiments, and find that NZSP is almost electrochemically stable with Na metal during cycling and it is not the key motivation for Na metal dendrite growth. We confirm that GBs properties mainly effect the Na metal dendrite growth in NZSP. By calculating the dynamically evolving local electric potential at GBs during Na dendrite growth via an electro-chemo-mechanically coupled phase-field (PF) model, we demonstrate that the GB properties play important roles in directing the Na metal dendrite growth rate and morphology evolution. Microscopic evidence is also provided for local properties of GBs to affect Na metal dendrite formation in NZSP. The local fluctuation of GB potential is very drastic (about 0.5 V), while as the applied d.c. current density is very low. The fluctuation of local GB potential could lead to the leakage because of the low work function (2.4 eV) of NZSP measured by UPS. The Na ion conductivity and mechanical strength of the GBs are found to be the main factors for the local Na dendrite growth kinetics. Based on our study model, tailoring GBs with sufficient Na ion/electron conductivity and Young's modulus is an effective route to suppress Na metal dendrite growth in polycrystalline SSEs. Given that the growth of Na dendrites results in considerable deformation, our subsequent work will integrate finite strain theory. This will enhance our understanding of the mechanical effects on Na dendrite growth. Additionally, in our upcoming research, we will delve into various solid electrolyte materials and examine their chemical and mechanical properties, and their impact on the Na dendrite growth.

4. Experimental Section

NZSP Pellets Synthesis and Surface Cleaning Treatment: The NASICON ($Na_3Zr_2Si_2PO_{12}$ stoichiometry) was prepared by a solid-state reaction.[16,34,37] The $Na_3Zr_2Si_2PO_{12}$ was prepared by mixing stoichiometric amounts of Na_2CO_3 (99.99%, Aladdin), ZrO_2 (AR, Sinopharm), $NH_4H_2PO_4$ (≥99.99%, Aladdin), SiO_2 (AR, Sinopharm), and Isopropanol (≥99.9%, Aladdin). 10 wt% excess Na_2CO_3 was added to compensate for sodium volatilization during high-temperature synthesis. After that, the mixture was subjected to a two-step heat treatment. The evenly mixed powder was heated at 950 °C for 4 h, with a temperature ramp-up rate of 5 °C min^{-1}. The calcined powders were manually ground using a pestle and mortar, followed by further grounding in a planetary ball mill in isopropanol for 7 h. Powder of 0.3 g every time was pressed using uniaxial pressing at about 7 MPa to form pellets of about 12 mm diameter and 0.9 ± 0.1 mm thickness. Next, calcination of the obtained pellets was performed at 1100 °C for 12 h with a temperature ramp-up rate of 5 °C min^{-1}. Extra mother powders of the same composition were placed both underneath and on the top of the pellets in the Al_2O_3 crucible. At last, both sides of prepared the NZSP pellets were polished to remove the contaminations from the top and bottom of each pellet to further ensure that the homogeneous and clean parts of the pellets were used for conductivity measurements and other experiments. X-ray diffraction patterns of the as-prepared $Na_3Zr_2Si_2PO_{12}$ were shown in Figure S10 (Supporting Information). The as-prepared $Na_3Zr_2Si_2PO_{12}$ sample shows high purity without other impurities; all the diffraction peaks can be indexed to a monoclinic structure (PDF 01-084-1200) with a space group of *C2/c*.

The heat treatment can clean the surface of NZSP. Heat treatment (450 °C in air) was used in this study to eliminate the by-product layer coating on the NZSP, which was generated on NZSP surface when it contacted with air (H_2O + CO_2). Heat treatment was carried out by placing the samples in an Al_2O_3 crucible and heating to temperatures at 450 °C in a muffle furnace (Kejing Corporation, China) for 2 h using 5 °C min^{-1} as heating rate. After this treatment, samples were transferred to an argon-filed glovebox for the following characterization.

Structure and Microstructure Characterizations of NZSP: The surface morphologies and cross-section view and EDS mapping of short-circuited NZSP were characterized by using a field-emission scanning electron microscope (SEM) (S4800 Hitachi, Japan). The NZSP and short-circuited NZSP pellets were cut by using FIB-SEM (Hitachi NX5000 ETHOS, Japan). The morphology and crystal structure of the NZSP short-circuited NZSP samples processed by FIB were then characterized by field emission TEM (JEM-2100F, Japan).

In Situ X-ray Imaging Cell (IXIcell) Assembly and Electrochemical Measurements: A thin Na wafer (Φ12 mm and about 0.1 mm thickness) was put on NZSP pellets in a glovebox filled with ultrahigh-purity argon (Ar), and then the stacked with a pressure in the IXIcell as shown in Figure S8 (Supporting Information), which designed by ourself and made by Gaossunion Corporation (Tianjin, China). In order to improve the solid-state contact between NZSP and Na metal, keep-loading-pressure perpendicular to the Na/NZSP/Na interface was set as about 15 MPa. All the assembly of Na/NZSP/Na symmetric cells were prepared with the same pressure. Moreover, the IXIcell was well sealed by using rubber ring and the inside of the cell filled with Ar gas. Electrochemical impedance spectroscopy (EIS) measurements were conducted by using a Gamary interface 1010E workstation between 1 MHz and 1 Hz at the amplitude of 10 mV. Galvanostatic cycling experiments of Na/NZSP/Na at a current density of 0.05, 0.1

0.2, 0.3 and 0.6 mA cm^{-2} were performed by using the Gamary interface 1020 workstation. All electrochemical measurements were taken at 25 °C outside the glove box, and EIS measurements were taken at various time intervals during the galvanostatic cycling.

EIS data were fitted with an equivalent circuit model consisting of a series connection of the following elements: a resistor (R_1), a parallel element consisting of a resistor (R_2), and constant phase element (Q). The resulting circuit was summarized: $(R_1Q) - (R_2Q)$. The high frequency arc (and offset resistance) represents the overall bulk Na ion transport (grain and grain boundary charge transfer resistance), and was modeled by the R_1 series contribution to the equivalent circuit model. The parallel (R_2Q) element models the contribution of NZSP/Na interface charge transfer resistance to the EIS spectrum.

Micro-XANES Measurement: The micro-XANES (μXANES) experiments were performed at the beamline I18 at the diamond light source (Harwell, UK). The beamline uses a cryogenically cooled Si (111) monochromator. The specialized designed cell was held in a plane to the incident beam, with the fluorescence detector positioned at 60–90° to the beam direction. In order to detect the average change and distribution of Zr along the NZSP/Na interface, the mapping method was used. The Zr K-edge μXANES mapping area was 63 μm × 25 μm in this study, with horizontal direction step size of 1 μm and vertical direction step size of 1 μm. The beam size was 2 μm × 2.5 μm, which was also the size of each pixel. Each μXANES mapping was consisting of 123 pieces of μXRF mappings collected at discrete energies from 17 960 to 18 124 (energy step: 2 eV for 17950-17070 and 18040–18124; 1 eV for 17 971 to 18 039). The data collection time for each pixel at one singal energy point was 0.02 seconds. For each μXANES mapping, 315 pixels at 123 different energies had a total collection time of 130 mins. The μXANES mapping were converted from the individual XRF map files recorded during the measurement into a format suitable for the program Mantis by using a python script.[45] The script integrates the XRF spectra mapping data for the selected energy window and divides it by the I0 reading at each point, generating and normalizing the XANES spectra. In Mantis, the XANES spectra was processed by using principal component analysis (PCA), which separate the mapping area by comparing the XANES spectra, and then cluster analysis was used to show the different XANES spectral associated with each region of the sample (e.g., interface and bulk for NZSP/Na).

Phase Field Models and Parameters: Phase-field simulation parameters and their normalized values are shown in **Table 1**. This study presents an electro-chemo-mechanical phase-field (PF) model for examining the growth of sodium dendrites in all-solid-state batteries (ASSB), while considering the grains and grain boundaries (GBs) through two distinct order parameters, η and β. The dendrite growth was assumed to occur from the nuclei to the entire domain, encompassing growth within grains and across GBs. The dendrite phase, representing sodium metal, was denoted by $\eta = 1$, while the solid-electrolyte (SE) phase was represented by $\eta = 0$. Additionally, the GB was designated as $\beta = 1$, with the grain phase, including the dendrite and SSE phases, represented by $\beta = 0$. The resulting system free energy can be expressed as:

Table 1. Phase-field simulation parameters and their normalized values.[47,48]

Parameters for the simulation		
Parameter name	Value	Unit
Maximum sodium ion concentration c_0	10^4	$mol\ m-3$
Maximum sites of sodium metal c_{max}	9.71×10^4	$mol\ m-3$
Ionic conductivity of sodium σ_{DE}	10^7	$s\ m-1$
Ionic conductivity of SE σ_{SE}	10^{-1}	$s\ m-1$
Energy barrier height W	3.6×10^6	$J\ m-3$
Diffusivity of sodium D_{Na}	1.5×10^{-16}	$m^2\ s-1$
Diffusivity of sodium ion D_{Na^+}	1.5×10^{-14}	$m^2\ s-1$
Phase mobility L	10^{-8}	$m^3J^{-1}s^{-1}$
Reaction rate L_c	0.6	s^{-1}

$$\psi = \psi_c + \psi_\eta + \psi_e + \psi_\phi + \psi_{grad} \tag{1}$$

where the chemical free energy ψ_c can be given as follows:

$$\psi_c = RTc_{max}c_{Na^+} \ln (c_{Na^+}) \tag{2}$$

with R and T being the gas constant and room temperature, c_{Na^+} was the normalized concentration of sodium-ions, c_{max} was the maximum concentration of Na^+ in the SE phase.

The double-well potential shown below can be used to describe the free energy associated with dendrite growth:

$$\psi_\eta = W\eta^2 (1-\eta)^2 = Wc_{Na}^2(1-c_{Na})^2 \tag{3}$$

where Equation 3 includes the energy barrier height coefficient, W. The order parameter for the dendrite phase was represented by $\eta = c_{Na}$, which indicates the normalized sodium concentration. The two minimal points correspond to the SE phase and dendrite phase, respectively, with $\eta = 0$ and $\eta = 1$. The interface between these two phases occurs at $0 < \eta < 1$, where the dendrite growth reaction takes place.

This study assumes that volume increase occurs due to dendrite growth (phase transformation from the SE phase to the dendrite phase), leading to an elastic free energy expression of the form:

$$\psi_e = \frac{1}{2}\boldsymbol{\sigma} : \boldsymbol{\varepsilon}_e, \quad \text{with } \boldsymbol{\sigma} = \mathbb{C}(\eta) : \boldsymbol{\varepsilon}_e, \quad \boldsymbol{\varepsilon}_e = \boldsymbol{\varepsilon} - \boldsymbol{\varepsilon}_p - \boldsymbol{\varepsilon}_\eta \tag{4}$$

where $\boldsymbol{\varepsilon}_\eta = \frac{\Omega}{3} h(\eta)\boldsymbol{I}$ denotes the volume expansion (dendrite growth) induced eigen strain, $\boldsymbol{\epsilon}_p$ represents the plastic strain, and Ω represents the volume change ratio/percentage from the SE phase to dendrite phase, and **I** was the identity tensor. It was worth noting that the elastic properties, such as the Young's modulus, of the dendrite phase (5 GPa) and the SE phase (50 GPa) differ significantly.[34] To ensure a smooth transition between phases, the phase-dependent elasticity tensor, $\mathbb{C}(\eta)$, has been employed.

This study has not considered anisotropic properties, such as polycrystalline sodium and anisotropic elastic constants, which will be addressed in future work. To simplify the analysis, the isotropic J2 plasticity model has been utilized to examine the elastoplastic response associated with dendrite growth. Given the significantly lower yield stress of sodium (≈ 0.5 MPa) in comparison to the NZSP phase (approximately 50 MPa), a phase-dependent yield condition has been introduced as follows:

$$f\left(\boldsymbol{\sigma}, \bar{\varepsilon}_{eff}, \eta\right) = \|dev[\boldsymbol{\sigma}]\| - \sqrt{\frac{2}{3}}\left(\sigma_Y(\eta) + H(\eta)\bar{\varepsilon}_{eff}\right) \tag{5}$$

where the yield stress $\sigma_Y(\eta)$ and the hardening moduli $H(\eta)$ were calculated by using the dendrite phase order parameter η, respectively. Here, the yield stress $\sigma_Y(\eta)$ and the hardening moduli $H(\eta)$ were calculated based on the dendrite phase order parameter, η. $dev[\sigma]$ and $\bar{\varepsilon}_{eff}$ respectively denote the deviatoric part of the Cauchy stress and the effective plastic strain. Next, the plastic flow can be given by:

$$\dot{\varepsilon}_p = \lambda \frac{dev[\sigma]}{\|dev[\sigma]\|} \tag{6}$$

$$\dot{\bar{\varepsilon}}_{eff} = \lambda\sqrt{\frac{2}{3}} \tag{7}$$

with λ being the plastic multiplier. It should be mentioned that, the smooth interpolation function $h(\eta) = \eta^3 (6\eta^3 - 15\eta + 10)$ has been used to calculate the phase-dependent quantities.

The electric free energy of the species takes the form

$$\psi_\phi = Fz_i c_i \tag{8}$$

with z_i and c_i being the charge number and concentration of i-th species, and F was the Faraday constant.

The gradient energy for the interface between phases (dendrite phase and SSE phase) can be read as follows:

$$\psi_{grad} = \frac{1}{2}\kappa \nabla^2 \eta \tag{9}$$

where the anisotropic gradient coefficient κ can be written as follows:[46]

$$\kappa = \kappa_0 [1 + \delta \cos(w\theta)] \tag{10}$$

The expression for the gradient energy includes the interface thickness constant, κ_0, and the anisotropy strength parameter, δ. The local angle, θ, for the dendrite growth was determined based on the gradient of the order parameter $\eta(\theta = \arctan(\frac{\partial\eta/\partial y}{\partial\eta/\partial x}))$, and the mode number for the anisotropy was represented by w.

In this work, the chemical reaction for the dendrite growth was considered as follows:

$$Na \Leftrightarrow Na^+ + e^- \tag{11}$$

where the reaction only occurs at the interface between Na dendrite phase and SSE phase was assumed, namely $0 < \eta < 1$. Then the chemical reaction at the interface can be read as follows:

$$I_{BV} = L_\eta h'(\eta) \left[\exp\left(\frac{\Delta G}{2RT}\right) - c_{Na^+} \exp\left(-\frac{\Delta G}{2RT}\right)\right] \tag{12}$$

with L_η being the reaction rate, ΔG was the active Gibbs energy constant for the reaction. $h'(\eta)$ was the 1st order derivative of $h(\eta)$, namely the double well function, this function restricts the reaction to occur solely at the interface ($0 < \eta < 1$).

Governing equations

The mass conservation of Na^+ can be read as follows:

$$\frac{\partial c_{Na^+}}{\partial t} = \nabla \cdot [D\nabla c_{Na^+} + Dc_{Na^+}\nabla\phi] - \frac{c_s}{c_{max}}\frac{\partial\eta}{\partial t} \tag{13}$$

The term D in the equation represents the diffusion coefficient of Na^+, a parameter dependent on phases that will be introduced later. c_s was the concentration of available sites in SE. To describe the evolution of dendrites, the following Allen-Cahn equation can be employed:

$$\frac{\partial\eta}{\partial t} = -L\frac{\partial\psi}{\partial\eta} + L\kappa\nabla^2\eta - L_\eta I_{BV} \tag{14}$$

It was worth noting that the term ψ encompasses contributions from both chemical processes (dendrite growth) and mechanical deformation (elastic free energy), resulting in the following expression:

$$\frac{\partial\psi}{\partial\eta} = \frac{\partial\psi_\eta}{\partial\eta} + \left[\mathbb{C} : (\varepsilon - \varepsilon_p - \varepsilon_\eta)\right] : \left(-\frac{\Omega}{3}h'(\eta)\boldsymbol{I}\right) \tag{15}$$

the second term on the right-hand side can be simplified to $-\Omega\sigma_h$, with $\sigma_h = tr(\sigma)$ being the hydrostatic stress (i.e., trace of the stress tensor).

The current in the Na dendrite phase and the NZSP SSE phase can be expressed as follows, based on Ohm's law:

$$\sigma_{DE}\nabla\phi = i_{DE} \tag{16}$$

and

$$\sigma_{SE}\nabla\phi = i_{SE} \tag{17}$$

Therefore, the mixed current through the phases can be expressed as:

$$i_{mix} = h(\eta) i_{DE} + (1 - h(\eta)) \; i_{SE} = \sigma_{mix}\nabla\phi \tag{18}$$

with $\sigma_{mix} = h(\eta)\sigma_{DE} + (1 - h(\eta))\sigma_{DE}$. Therefore, the equation governing the electric field can be expressed as:

$$\nabla \cdot (\sigma_{mix}\nabla\phi) = Fc_s\dot{\eta} \tag{19}$$

where the ionic conductivity σ_{mix} depends on both η and β, and will be introduced later. In the end, the stress equilibrium was solved via:

$$\nabla \cdot \boldsymbol{\sigma} = 0 \tag{20}$$

Boundary Conditions: It was worth noting that the Dirichlet boundary condition has been applied to the sodium-ions on the right-hand side of the sample to ensure the Na-ion was always available at the right edge. To obtain the solution of the Poisson equation, the potential on the right-side edge has been set to zero.

Material Properties in Grains and GB: Given that the system includes both grains and GBs, different properties can be assigned to these two domains using the interpolation function h(x). For example, the diffusion coefficients in the dendrite phase (D_{DE}), SSE phase (D_{SE}), and grain boundary (D_{GB}) may differ. As such, the diffusion coefficient for the grain was expressed as follows:

$$D_{GR} = h(\eta) D_{DE} + (1 - h(\eta)) D_{SE} \tag{21}$$

Then the final diffusion coefficient of Na^+ can be read as follows:

$$D = h(\beta) D_{GB} + (1 - h(\beta)) [h(\eta) D_{DE} + (1 - h(\eta)) D_{SE}] \tag{22}$$

In a similar manner, the Young's modulus E and the ionic conductivity σ_{mix} can be expressed as follows:

$$E = h(\beta) E_{GB} + (1 - h(\beta)) [h(\eta) E_{DE} + (1 - h(\eta)) E_{SE}] \tag{23}$$

and

$$\sigma_{mix} = h(\beta) \sigma_{GB} + (1 - h(\beta)) [h(\eta) \sigma_{DE} + (1 - h(\eta)) \sigma_{SE}] \tag{24}$$

Supporting Information

Supporting Information is available from the Wiley Online Library or from the author.

Acknowledgements

This work was supported by the National Natural Science Foundation of China (No. 5202780089). The authors acknowledge Diamond Light Source beamtime (SP29192, SP30403, and I09 session). The author would like to thank Dr. Stuart Bartlett in I18 of Diamond light source for his numerous help during the experiment and data analysis. Z.G. acknowledges support from the Chinese Scholarship Council (CSC).

Conflict of Interest

The authors declare no conflict of interest.

Author Contributions

Z.G., Y.B., J.F. contributed equally to this work. All authors have given approval to the final version of the manuscript.

Data Availability Statement

Research data are not shared.

Keywords

grain boundaries, interface, NASICON, sodium dendrite, solid-state battery

Received: December 25, 2023
Revised: January 29, 2024
Published online: February 26, 2024

[1] Z. Gao, H. Sun, L. Fu, F. Ye, Y. Zhang, W. Luo, Y. Huang, *Adv. Mater.* **2018**, *30*, 1705702.
[2] Y. Xiao, Y. Wang, S.-H. Bo, J. C. Kim, L. J. Miara, G. Ceder, *Nat. Rev. Mater.* **2019**, *5*, 105.
[3] C. Zhao, L. Liu, X. Qi, Y. Lu, F. Wu, J. Zhao, Y. Yu, Y.-S. Hu, L. Chen, *Adv. Energy Mater.* **2018**, *8*, 1703012.
[4] J. Cui, A. Wang, G. Li, D. Wang, D. Shu, A. Dong, G. Zhu, J. Luo, B. Sun, *J. Mater. Chem. A* **2020**, *8*, 15399.
[5] J. Janek, W. G. Zeier, *Nat. Energy* **2016**, 16141. https://doi.org/10.1038/NENERGY.2016.141
[6] T. Ortmann, S. Burkhardt, J. K. Eckhardt, T. Fuchs, Z. Ding, J. Sann, M. Rohnke, Q. Ma, F. Tietz, D. Fattakhova-Rohlfing, C. Kübel, O. Guillon, C. Heiliger, J. Janek, *Adv. Energy Mater.* **2023**, 13, 2202712.
[7] Q. Ma, M. Guin, S. Naqash, C.-L. Tsai, F. Tietz, O. Guillon, *Chem. Mater.* **2016**, *28*, 4821.
[8] M. Guin, F. Tietz, *J. Power Sources* **2015**, *273*, 1056.
[9] S. Lou, F. Zhang, C. Fu, M. Chen, Y. Ma, G. Yin, J. Wang, *Adv. Mater.* **2021**, *33*, 2000721.
[10] S. Wang, H. Xu, W. Li, A. Dolocan, A. Manthiram, *J. Am. Chem. Soc.* **2018**, *140*, 250.
[11] T. Famprikis, P. Canepa, J. A. Dawson, M. S. Islam, C. Masquelier, *Nat. Mater.* **2019**, *18*, 1278.
[12] J. Kasemchainan, S. Zekoll, D. S. Jolly, Z. Ning, G. O. Hartley, J. Marrow, P. G. Bruce, *Nat. Mater.* **2019**, *18*, 1105.
[13] Y. Lu, C. Z. Zhao, H. Yuan, X. B. Cheng, J. Q. Huang, Q. Zhang, *Adv. Funct. Mater.* **2021**, *31*, 2009925.
[14] X. Han, Y. Gong, K. K. Fu, X. He, G. T. Hitz, J. Dai, A. Pearse, B. Liu, H. Wang, G. Rubloff, Y. Mo, V. Thangadurai, E. D. Wachsman, L. Hu, *Nat. Mater.* **2017**, *16*, 572.
[15] J. Yang, Z. Gao, T. Ferber, H. Zhang, C. Guhl, L. Yang, Y. Li, Z. Deng, P. Liu, C. Cheng, R. Che, W. Jaegermann, RenéHausbrand, Y. H., *J. Mater. Chem. A* **2020**, *8*, 7828.
[16] J. Yang, H. Xu, J. Wu, Z. Gao, F. Hu, Y. Wei, Y. Li, D. Liu, Z. Li, Y. Huang, *Small Methods* **2021**, *5*, 2100339.
[17] T. Krauskopf, H. Hartmann, W. G. Zeier, J. Janek, *ACS Appl. Mater. Interfaces* **2019**, *11*, 14463.
[18] H. Tang, Z. Deng, Z. Lin, Z. Wang, I.-H. Chu, C. Chen, Z. Zhu, C. Zheng, S. P. Ong, *Chem. Mater.* **2017**, *30*, 163.
[19] M. J. Wang, R. Choudhury, J. Sakamoto, *Joule* **2019**, *3*, 2165.
[20] Z. Ning, D. S. Jolly, G. Li, R. De Meyere, S. D. Pu, Y. Chen, J. Kasemchainan, J. Ihli, C. Gong, B. Liu, D. L. R. Melvin, A. Bonnin, O. Magdysyuk, P. Adamson, G. O. Hartley, C. W. Monroe, T. J. Marrow, P. G. Bruce, *Nat. Mater.* **2021**, *20*, 1121.
[21] X. Liu, R. Garcia-Mendez, A. R. Lupini, Y. Cheng, Z. D. Hood, F. Han, A. Sharafi, J. C. Idrobo, N. J. Dudney, C. Wang, C. Ma, J. Sakamoto, M. Chi, *Nat. Mater.* **2021**, *20*, 1485.
[22] S. Yu, D. J. Siegel, *Chem. Mater.* **2017**, *29*, 9639.
[23] L. Porz, T. Swamy, B. W. Sheldon, D. Rettenwander, T. Frömling, H. L. Thaman, S. Berendts, R. Uecker, W. C. Carter, Y. M. Chiang, *Adv. Energy Mater.* **2017**, *7*, 1701003.
[24] S. Yu, D. J. Siegel, *ACS Appl. Mater. Interfaces* **2018**, *10*, 38151.
[25] B. S. Vishnugopi, M. B. Dixit, F. Hao, B. Shyam, J. B. Cook, K. B. Hatzell, P. P. Mukherjee, *Adv. Energy Mater.* **2022**, *12*, 2102825.
[26] C. Yuan, X. Gao, Y. Jia, W. Zhang, Q. Wu, J. Xu, *Nano Energy* **2021**, *86*, 106057.
[27] C. Yuan, W. Lu, J. Xu, *Adv. Energy Mater.* **2021**, *11*, 2101807.
[28] H.-K. Tian, Z. Liu, Y. Ji, L.-Q. Chen, Y. Qi, *Chem. Mater.* **2019**, *31*, 7351.
[29] F. Han, A. S. Westover, J. Yue, X. Fan, F. Wang, M. Chi, D. N. Leonard, N. J. Dudney, H. Wang, C. Wang, *Nat. Energy* **2019**, *4*, 187.
[30] K. Shen, R. He, Y. Wang, C. Zhao, H. Chen, *J. Phys. Chem. C* **2020**, *124*, 26241.
[31] B. Gao, R. Jalem, H. K. Tian, Y. Tateyama, *Adv. Energy Mater.* **2022**, *12*, 2102151.
[32] K. Tantratian, H. Yan, K. Ellwood, E. T. Harrison, L. Chen, *Adv. Energy Mater.* **2021**, *11*, 2003417.
[33] E. Kazyak, R. Garcia-Mendez, W. S. LePage, A. Sharafi, A. L. Davis, A. J. Sanchez, K.-H. Chen, C. Haslam, J. Sakamoto, N. P. Dasgupta, *Matter* **2020**, *2*, 1025.
[34] Z. Gao, J. Yang, G. Li, T. Ferber, J. Feng, Y. Li, H. Fu, W. Jaegermann, C. W. Monroe, Y. Huang, *Adv. Energy Mater.* **2022**, *12*, 2103607.
[35] J. Fleig, *Solid State Ionics* **2002**, *150*, 181.
[36] Y. Ren, Y. Shen, Y. Lin, C.-W. Nan, *Electrochem. Commun.* **2015**, *57*, 27.
[37] Z. Gao, J. Yang, H. Yuan, H. Fu, Y. Li, Y. Li, T. Ferber, C. Guhl, H. Sun, W. Jaegermann, R. Hausbrand, Y. Huang, *Chem. Mater.* **2020**, *32*, 3970.
[38] L. Brinza, P. F. Schofield, M. E. Hodson, S. Weller, K. Ignatyev, K. Geraki, P. D. Quinn, J. F. Mosselmans, *J. Synchrotron Radiat.* **2014**, *21*, 235.
[39] Y. Zhu, X. He, Y. Mo, *ACS Appl. Mater. Interfaces* **2015**, *7*, 23685.
[40] S. P. Ong, Y. Mo, W. D. Richards, L. Miara, H. S. Lee, G. Ceder, *Energy Environ. Sci.* **2013**, *6*, 148.
[41] G. Mountjoy, D. M. Pickup, R. Anderson, G. W. Wallidge, M. A. Holland, R. J. Newport, M. E. Smith, *Phys. Chem. Chem. Phys.* **2000**, *2*, 2455.
[42] F. Meneghetti, E. Wendel, S. Mascotto, B. M. Smarsly, E. Tondello, H. Bertagnolli, S. Gross, *CrystEngComm* **2010**, *12*, 1639.
[43] P. Li, I.-W. Chen, J. E. Penner-Hahn, X-ray-absorption studies of zirconia polymorphs. I. Characteristic local structures. **1993**, 48.
[44] U. C. Srivastava, H. L. Nigam, *Coord. Chem. Rev.* **1972**, *9*, 275.
[45] M. Lerotic, R. Mak, S. Wirick, F. Meirer, C. Jacobsen, *J. Synchrotron Radiat.* **2014**, *21*, 1206.
[46] L. Chen, H. W. Zhang, L. Y. Liang, Z. Liu, Y. Qi, P. Lu, J. Chen, L.-Q. Chen, *J. Power Sources* **2015**, *300*, 376.
[47] L. Gao, Z. Guo, *Comput. Mater. Sci* **2020**, *183*, 109919.
[48] L. Liang, L.-Q. Chen, *Appl. Phys. Lett.* **2014**, *105*, 263903.